Surface Topography: Metrology and Properties

RECEIVED
18 November 2020

REVISED
5 February 2021

ACCEPTED FOR PUBLICATION
21 April 2021

PUBLISHED
5 May 2021

PAPER

Extension and validation of a revised Cassie-Baxter model for tailor-made surface topography design and controlled wettability

Nikolaos Lempesis[1,2,*], **Rudolf J Koopmans**[1,2], **Ruth Díez-Ahedo**[3] and **Per Magnus Kristiansen**[4,5,6]

[1] Plastics Innovation Competence Center, Passage du Cardinal 1, CH-1700 Fribourg, Switzerland
[2] Department of Mechanical Engineering, College of Engineering and Architecture Fribourg HES-SO, Bd de Pérolles 80, CH-1705 Fribourg, Switzerland
[3] Tekniker, Iñaki Goenaga 5, 20600 Eibar, Spain
[4] FHNW University of Applied Sciences and Arts Northwestern Switzerland, School of Engineering, Institute of Polymer Nanotechnology (INKA), Klosterzelgstrasse 2, CH-5210 Windisch, Switzerland
[5] Laboratory for Micro- and Nanotechnology, Paul Scherrer Institute, 5232 Villigen PSI, Switzerland
[6] University College Dublin, School of Mechanical and Material Engineering, Belfield, Dublin 4, Ireland
[*] Author to whom any correspondence should be addressed.

E-mail: nikolaos.lempesis@hefr.ch **and** nic.0s@hotmail.com

Keywords: wettability, topography, Cassie-Baxter, wetting model, hydrophobic, omniphobic

Supplementary material for this article is available online

Abstract

Predicting wettability accurately across various materials, surface topographies and wetting liquids is undeniably of paramount importance as it sets the foundations for technological developments related to improved life quality, energy saving and economization of resources, thereby reducing the environmental impact for recycling and reuse. In this work, we extend and validate our recently published wetting model, constituting a refinement of the original Cassie-Baxter model after consideration of realistic curved liquid-air interfaces. Our model enabled more meaningful contact angle predictions, while it captured the experimentally observed trends between contact angle and surface roughness. Here, the formalism of our wetting model is further extended to 3D surface topographies, whereas the validity of our model, in its entirety, is evaluated. To this end, a total of thirty-two experimentally engineered surfaces of various materials exhibiting single- and multilevel hierarchical topographies of increasing complexity were utilized. Our model predictions were consistently in remarkable agreement with experimental data (deviations of 3%–6%) and, in most cases, within statistical inaccuracies of the experimental measurements. Direct comparison between experiments and modeling results corroborated that surface topographies featuring re-entrant geometries promoted enhanced liquid-repellency, whereas hierarchical multilevel surface topographies enabled even more pronounced nonwetting behaviors. For the sinusoidal topography, consideration of a second superimposing topography level almost doubled the observed water contact angles, whereas addition of a third level brought about an extra 12.5% increase in water contact angle.

1. Introduction

Everyday life commodities, such as food, water and other beverages, as well as inedible domestic products, such as cosmetics and liquid detergents are stored, transported and maintained within plastic or glassy containers. Adhesion of these goods to their packaging material is responsible for product waste [1], poor product appearance [2], increased package recycling costs [3], as well as sanitary problems and production deterioration in industrial units due to fouling of equipment [4]. Wettability was identified as the most dominant mechanism related to adhesion of a liquid onto a solid surface. This mechanism described the interactions between a liquid and a solid surface and was quantified, at mechanical equilibrium, by means of the apparent contact angle θ, also referred to as static contact angle [5]. Liquid-repellent surfaces exhibited increased resistance to wetting which translated into large values for θ. Controlling wettability of a surface

proved to be a valuable tool for the design of numerous engineering applications including hydrophobic [6, 7] or oleophobic [8] non-wetting textiles, anti-fogging [9] and anti-icing [10] technologies, optimized buoyancy [11] and associated flow improvement [12], as well as antibiofouling [13] and water collection from fog [14].

Despite numerous applications invoking the theoretical underpinnings of wettability, understanding and controlling it remains largely still elusive thereby constituting a perpetual struggle for scientist, in which, luckily, they are not alone. To the observant enough and with keen perceptiveness, nature proved to be a valuable ally exemplifying numerous cases of biological surfaces with remarkable wetting behavior. In the relatively recently spawned and rapidly developing fields of biomimetics and bionics, applications were engineered with functions emulating everyday behavior of such biological systems. Prominent examples of such influential bioinspired-surfaces and resulting technological applications included non-reflective surfaces utilizing the 'moth-eye' effect [15], inspection robots with highly adhesive surfaces making use of the 'gecko-effect' [16, 17], self-cleaning window panes using the 'lotus leaf effect' [18], solid bodies exhibiting improved flowability owed to reduced drag by exploiting the 'shark skin effect' [19, 20], as well as numerous other emerging applications related to energy conversion and conservation [21].

The difficulty to comprehend wettability fully was, in large part, attributed to the great number of parameters contributing to the intricacy of the phenomenon, including surface chemistry [22, 23], surface roughness [24, 25], temperature [26], mechanical loading [27], crystallinity [28] and applied electric field [29, 30]. Chemistry modifications of the surface, albeit promising, proved to have rather limited effect on wettability [31]. In contrast, changes in the surface topography appeared a more efficient way for manipulating wettability, even for the design of oil-repellent surfaces [32]. For even more pronounced control over wettability, very recently, topography modifications were combined efficiently with chemical treatment of various surfaces including cotton [33, 34], steel [35] and synthetic leather [36]. Further examples include trichloro(1H,1H,2H,2H-perfluorooctyl) silane (PFOCTS)-modified cobalt structures for creating omniphobic surfaces [37], Cd-Si co-doped TiO_2 thin films examining the synergistic effect of co-dopants and calcination temperature on wettability [38], as well as polymer nanocomposite surfaces comprising Au/ZnO nanoparticles randomly dispersed in a cellulose acetate polymer matrix [39]. A detailed compilation of substrate coatings and associated fabrication techniques can be found in the comprehensive work of B Bhushan and S Martin [40].

In the general context of tinkering surface topography, surface roughness was of paramount importance [32, 41]. Extensive studies on biological surfaces, such as the leaves of *Ginkgo biloba* [25] and *Nelumbo nucifera* (lotus) [42] plants elaborated on the effect of roughness on overall nonwetting capabilities. The superhydrophobic traits of these biological surfaces were attributed initially to their distinct surface roughness which theoretically rendered them in a metastable state. This assumption was later on confirmed in the pioneering works of Marmur [43] and Nosonovsky [44]. Subsequently, an analysis entailing Gibbs surface free energy minimization in various solid-liquid-air systems showed that wetting states were distinct and could indeed be metastable and rather long-lived [45]. Besides surface roughness, biological surfaces often exhibited hierarchical organization, i.e., multiple levels of surface topographies placed on top of each other, which, in turn, was responsible for increased surface roughness owed to larger surface-to-volume ratio. A characteristic example was the morphology of the lotus leaves comprising nanoscale roughness superimposed over microscale bumps [46]. Hierarchical topographies in biological surfaces were, in many instances, identified to promote liquid repellency [47, 48].

Engineered surfaces, on the other hand, differed, in many cases considerably, from biological surfaces due to multilevel hierarchical organization customarily present in the latter. This was because implementing multilevel topographies of multiplicity larger than two on engineered surfaces constituted a formidable technological challenge. Interestingly, non-hierarchical surfaces, which, however, retained some degree of roughness, displayed superhydrophobicity [49]. In addition, water-repelling surfaces were produced without necessarily featuring hierarchical topography [50, 51]. Therefore, in total, roughness was seemingly more important than hierarchical organization (multilevel topography), the latter being, however, beneficial for enhanced liquid-repellency.

Modelling wettability played a decisive role in the design of surface topographies with tailored properties, as well as in the interpretation of experimental observations. Ever since the inaugural modelling attempts undertaken by Thomas Young in 1805 [52], followed by Wenzel [53] and eventually by Cassie and Baxter [54], numerous theoretical works emerged [55–60] thereby manifesting the great technological potential associated with increased wettability control. Without any loss of generality and for simplicity, most of these models considered only two-dimensional (2D) systems, implying that the surface texture extended to infinity along the remaining dimension forming thus a semi-infinite three-dimensional (3D) representation. This practice was customary and was shown to produce results in gratifying agreement with realistic 3D measurements [61, 62]. Most of these works made use of the classical Cassie-Baxter (CB) model or some variation of it, assuming thus that the liquid-air interface was a straight line. Usually, this

held true because of the typically small distance between neighboring surface irregularities.

Complementing seminal works trying to address this issue [63–66], in our recent study [67], we revoked this constraint by deriving the formalism of a refined CB model which, nonetheless, considered curved liquid-air interfaces on various single- and two-level topographies. Direct comparison between our model and the original CB model revealed that the latter overpredicted substantially the contact angle, while it failed to capture the anticipated trends between contact angle and roughness. Because of this deviating behavior, the original CB model did not capture the transitions from the CB state to the Wenzel and Young states with decreasing surface roughness.

2. Materials and methods

Throughout this work, the basis of the calculations was our refined CB model derived and applied for the predictions of surface topographies exhibiting superomniphobic traits [67]. The heart of our methodology lay in the consideration of realistic curved liquid-air interfaces separating trapped air from supernatant liquid. The radius of the curved meniscus was defined with the help of the capillary length $l_{cap} = \sqrt{\gamma_{la}/\rho g}$, which was, in turn, a function of the liquid surface tension γ_{la}, the liquid density ρ and the gravitational acceleration g. The curvature of the liquid-air interface was then quantified by considering the sagging (or protrusion) height $h = l/l_{cap}$, where l was a characteristic topography-dependent length. For all considered single-level surface topographies, l was defined accordingly [67].

By observing the original CB model, $\theta^{CB} = f_{sl}\cos\theta^{Y} - f_{la}$, where f_{sl} and f_{la} describe the area fractions of the solid-liquid and liquid-air interfaces, respectively, and the superscript Y denotes the contact angle by virtue of Young's relation [52], it becomes obvious that the calculation of θ^{CB} depends on f_{sl} and f_{la}, which, in turn, depend on the surface topography type and the shape of the liquid-air interface. Correspondingly, in our previous work [67], analytical expressions for f_{sl} and f_{la} were derived for the 2D pillars, fiber and sinusoidal surface topographies illustrated in figures 1(a)–(c), respectively. In addition, a generic algebraic expression for modeling multilevel hierarchical roughness of arbitrarily large multiplicity was derived based on information on single-level roughness. This expression was employed here to predict the water contact angle on hierarchical two- and three-level topographies.

Our model requires as input physicochemical parameters of the wetting liquid (density ρ and surface tension γ_{la}), Young contact angle θ^{Y} of the wetting liquid on a completely flat and smooth surface made of the same material as the rough surface, as well as type and dimensionality of surface topography. The Young contact angle can be measured experimentally, or, alternatively, it can be computed by virtue of the Young equation $\cos\theta^{Y} = (\gamma_s - \gamma_{sl})/\gamma_{la}$, where γ_s and γ_{la} are the solid surface energy and liquid surface tension terms, respectively, which can be measured experimentally or be found in material databases. The remaining interfacial surface energy term γ_{sl} cannot be measured directly and thus needs to be computed by using any of the conventional Fowkes [68], Zisman [69] or Owens-Wendt [70] theoretical approximations, with the latter being slightly preferential over the others. Should this be the case, information on the polar and dispersive components of γ_{la} and γ_s is required. Here, the Young contact angle was measured experimentally or, where applicable, was found in the literature (see below) and thus there was no need to resort to measuring the polar and dispersive parts of γ_{la} and γ_s.

The objective of the current work was twofold: on one side, we extended the formalism of our refined CB model from semi-infinite 2D to 3D topographies, whereas, on the other side, we tested and validated our model, in its entirety, by comparing directly model predictions with experimental data for various combinations of surface topographies, hierarchy levels and surface materials. Accordingly, area fractions f_{sl} and f_{la} were derived for a new 3D surface topography featuring 3D pillars with square cross section. A schematic illustration of this new single-level topography, along with its characteristic geometric details are shown in figure 1(d). The resulting area fraction relations for this topography are as follows (see supplementary material for derivation (available online at stacks.iop.org/STMP/9/025021/mmedia)):

$$f_{sl} = \frac{W^2}{D_p^2} \tag{1}$$

$$f_{la} = \frac{2l_{arc}W + (l_{arc})^2}{D_p^2} \tag{2}$$

where W and D_p represent the width and unit cell distance (see figure 1(d)) and l_{arc} is the numerator of the corresponding f_{la} relation for 2D pillars as it was derived in our recent work for different wetting cases, i.e., wetting liquid touches (wets) the surface base level or not [67].

To validate our model, totally eleven single-level surface topographies of various dimensions and types were considered in full compliance with the three basic surface topographies introduced originally [67], namely 2D flat-top pillars (figure 1(a)), fibers with circular cross-section (figure 1(b)) and sinusoids (figure 1(c)). To further validate the ability of our model to capture accurately wetting of surfaces with 3D texture, additionally eight 3D-pillar topographies of various dimensions were used for a total of nineteen single-level surface topographies (2D and 3D). Figures 1(e)–(h) describe representative experimental surfaces displaying 2D-pillar, sinusoidal and 3D-pillar

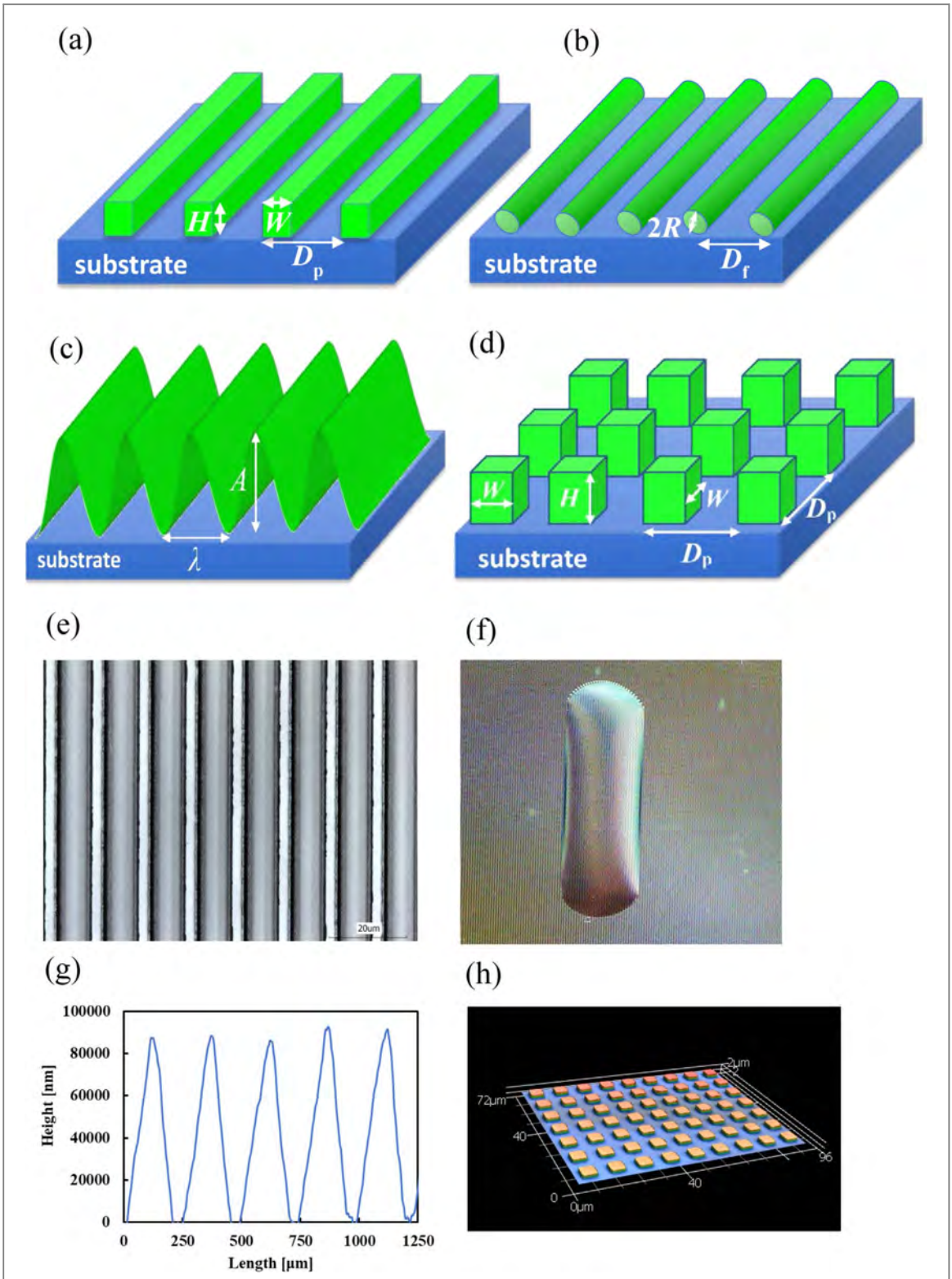

Figure 1. Schematic illustration of single-level (a) 2D-pillar, (b) fiber, (c) sinusoidal and (d) 3D-pillar topographies. Relevant geometric parameters are also shown. (e) Confocal laser scanning microscopy (CLSM) top view of a representative 2D-pillar topography corresponding to structure 4 in table 1, (f) pronounced anisotropic wetting by water (picture taken from underneath the wetted sample of part (e), (g) Profile of an indicative sinusoidal topography corresponding to structure 9 in table 1 measured by a mechanical profilometer (Veeco Dektrak-8 with 0.7 μm tip) and (h) CSLM 3D view of a representative 3D-pillar topography corresponding to structure 13 in table 1.

topography, respectively. Furthermore, to validate our model predictions related to multilevel topography, twelve two-level and one three-level hierarchical surfaces were studied. Representative 2D schematic illustrations of the two- and three-level surface topographies considered here are shown in figure 2. Accordingly, figure 2(a) illustrates the 'pillars on sinusoids' topography corresponding to structures 20–22 in table 2, figure 2(b) shows the 'sinusoids on sinusoids' topography describing structures 23–31 in

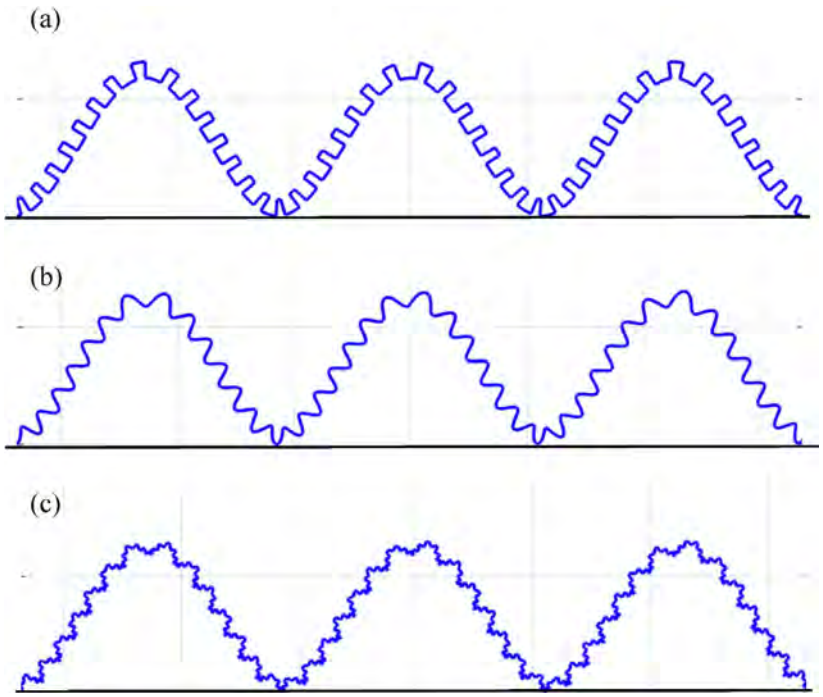

Figure 2. Representative 2D schematic illustrations of the hierarchical two-level (a) pillars on sinusoids, (b) sinusoids on sinusoids and (c) three-level triple sinusoidal surface topographies described in table 2.

Table 1. Description of single-level surface topographies considered here. Symbols H, W and D_p correspond to pillar height, width and unit cell distance, respectively, whereas R and D_f describe the fiber radius and unit cell distance, respectively. Finally, A and λ represent the amplitude and wavelength of the sinusoidal topography, respectively. Experimental Young's contact angle θ^Y of water on each surface is also reported.

Structure #	Topography	Dimensions [μm]	Surface material	θ^Y [°]	References
1	2D Pillars	$H = 0.253, W = 25, D_p = 50$	silanized silicon wafer	116.7	this work
2	2D Pillars	$H = 0.253, W = 50, D_p = 100$	silanized silicon wafer	116.7	this work
3	2D Pillars	$H = 0.253, W = 100, D_p = 200$	silanized silicon wafer	116.7	this work
4	2D Pillars	$H = 4.4, W = 3.4, D_p = 12$	PLGA	72.7	this work & [71]
5	2D Pillars	$H = 10, W = 45.5, D_p = 90.6$	COC	88.3	[72]
6	fibers	$R = 18, D_f = 79$	PDMS	105	[8]
7	fibers	$R = 12.5, D_f = 63$	PDMS	105	[8]
8	fibers	$R = 14, D_f = 78$	PDMS	105	[8]
9	sinusoidal	$A = 86, \lambda = 225$	aluminium	67.1	this work
10	sinusoidal	$A = 96, \lambda = 280$	aluminium	67.1	this work
11	sinusoidal	$A = 90, \lambda = 480$	aluminium	67.1	this work
12	3D Pillars	$H = 1.6, W = 2.6, D_p = 3.9$	COC	93	this work
13	3D Pillars	$H = 1.7, W = 6.0, D_p = 10.4$	COC	93	this work
14	3D Pillars	$H = 1.8, W = 3.9, D_p = 6.6$	COC	93	this work
15	3D Pillars	$H = 8.6, W = 44.7, D_p = 90.6$	COC	88.3	[72]
16	3D Pillars	$H = 8.0, W = 45.5, D_p = 90.6$	COC	88.3	[72]
17	3D Pillars	$H = 10.0, W = 10.0, D_p = 20.0$	SMP	89	[73]
18	3D Pillars	$H = 10.0, W = 10.0, D_p = 30.0$	SMP	89	[73]
19	3D Pillars	$H = 10.0, W = 10.0, D_p = 40.0$	SMP	89	[73]

table 2, whereas figure 2(c) displays the 'triple sinusoidal' topography of structure 32 in table 2. A detailed description of the characteristic geometrical parameters of the experimental single- and multilevel surface topographies considered here is provided in tables 1 and 2, respectively. Given the great technological importance of surfaces exhibiting patterns of diverse length scales, caution was taken here that a broad spectrum of characteristic lengths was spanned ranging from a few hundreds of micrometers to a few tens of nanometers (cf. tables 1 and 2). This corroborates the generic validity and applicability of our model.

Throughout this work, the wetting liquid was water having density ρ and surface tension γ_{la} at ambient conditions equal to 997 kg m^{-3} and 72.8 mN m^{-1}, respectively. To extract conclusions on the generic character of our model, a rich variety of surface

Table 2. Description of hierarchical multilevel surface topographies considered here. Symbols are identical to table 1. Subscripts 1, 2 and 3 (where applicable) denote different levels starting from the finest towards coarser ones. Experimental Young's contact angle θ^Y of water on each surface is also reported.

Structure #	Topography	Dimensions [μm]	Surface material	θ^Y [°]	References
20	pillars on sinusoids	$H = 0.15, W = 0.3, D_p = 0.5$ $A = 4.4, \lambda = 31$	PDMS	110	[74]
21	pillars on sinusoids	$H = 0.35, W = 0.2, D_p = 0.5$ $A = 4.4, \lambda = 31$	PDMS	110	[74]
22	pillars on sinusoids	$H = 0.7, W = 0.15, D_p = 0.5$ $A = 4.4, \lambda = 31$	PDMS	110	[74]
23	sinusoids on sinusoids	$A_1 = 0.275, \lambda_1 = 0.822$ $A_2 = 0.6, \lambda_2 = 25$	PDMS	119	[75]
24	sinusoids on sinusoids	$A_1 = 0.322, \lambda_1 = 0.774$ $A_2 = 2.75, \lambda_2 = 39$	PDMS	119	[75]
25	sinusoids on sinusoids	$A_1 = 0.305, \lambda_1 = 0.79$ $A_2 = 3.5, \lambda_2 = 39$	PDMS	119	[75]
26	sinusoids on sinusoids	$A_1 = 0.311, \lambda_1 = 0.825$ $A_2 = 4.35, \lambda_2 = 34$	PDMS	119	[75]
27	sinusoids on sinusoids	$A_1 = 0.247, \lambda_1 = 0.77$ $A_2 = 2.5, \lambda_2 = 16.7$	PDMS	119	[75]
28	sinusoids on sinusoids	$A_1 = 0.297, \lambda_1 = 0.8$ $A_2 = 4.5, \lambda_2 = 25.8$	PDMS	119	[75]
29	sinusoids on sinusoids	$A_1 = 0.27, \lambda_1 = 0.776$ $A_2 = 3.75, \lambda_2 = 20$	PDMS	119	[75]
30	sinusoids on sinusoids	$A_1 = 0.315, \lambda_1 = 0.815$ $A_2 = 4.5, \lambda_2 = 23.3$	PDMS	119	[75]
31	sinusoids on sinusoids	$A_1 = 0.267, \lambda_1 = 0.75$ $A_2 = 4.2, \lambda_2 = 21.4$	PDMS	119	[75]
32	triple sinusoidal	$A_1 = 0.075, \lambda_1 = 0.15$ $A_2 = 0.45, \lambda_2 = 0.9$ $A_3 = 5, \lambda_3 = 10$	PDMS	110	[76]

materials was considered involving silanized silicon wafers, poly(lactic-*co*-glycolic) acid (PLGA) comprising 85% polylactic acid (PLA) and 15% polyglycolic acid (PGA), cyclic olefin copolymer (COC), polydimethylsiloxane (PDMS), aluminium and an epoxy-based shape memory polymer (SMP). Structures 1–3 in table 1 were fabricated on silicon wafers using standard UV-lithographic techniques. Briefly, silicon wafers were spin-coated with a positive photoresist and exposed to UV light in an EVG 620 mask aligner using a designed chromium-on-glass photomask. After photoresist development, a Deep Reactive Ion Etching (DRIE) process was carried out in an Oxforf Plasmalab 80 + machine to etch the silicon in the areas not covered by the photoresist. After etching, the remaining photoresist was removed by successive sonication in acetone, IPA and deionized water.

Then, the wafer was fluorinated by exposure for 30 min to a saturated atmosphere of vapor PFOCTS. Structures 9–11 were fabricated using a picosecond laser Nd:YVO4 (3D MicroMac Microstruct) with pulses of 10 ps and wavelength of 1064, 532 and 355 nm, respectively. Therein, the beam diameter was smaller than 30 μm. Contact angle measurements for structures 1–3 and 9–11 were performed on a Surftens universal (OEG) goniometer. Analogously, polymer-based surface topographies 4 and 12–14 were fabricated by hot embossing on a Jenoptik HEX 03 using a silicon wafer with test patterns manufactured by photolithography and subsequent etching. Hot embossing was carried out at 100 °C for PLGA and at 120 °C for COC. Water contact angle measurements were performed on a Krüss drop shape analyzer (DSA 100).. For all surfaces constructed in the context of this work (cf. table 1), the Young contact angle of water was measured with the help of the goniometers reported above.

3. Results and discussion

3.1. Single-level topographies

Figures 3 and 4 illustrate comparisons between calculated contact angles and their experimental counterparts for the nineteen single-level surface topographies listed in table 1. In particular, figure 3 shows contact angle comparisons for 2D pillars, fibers, and sinusoidal topographies, whereas figure 4 for 3D pillars. For the 2D pillars case, depicted in figure 3, the agreement between experiment and model was gratifying resulting to an average error of about 6%. This was, at least partially, attributed to the inherent assumption of our model pertaining to pinning of the liquid at the corners of the pillars. This assumption hampered the droplet from intruding in the free space between neighboring pillars thus causing artificially increased contact angles as evinced by figure 3. Nonetheless, this discrepancy lay for three of the totally five

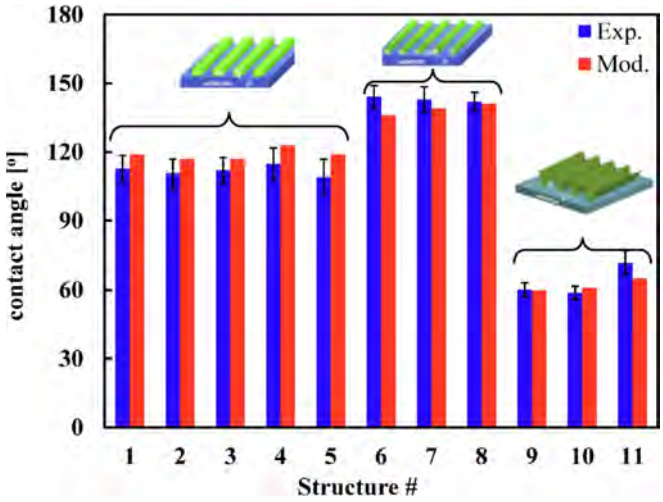

Figure 3. Contact angle comparison between model results (red) and experimental data (blue) for eleven single-level topographies: structures 1–5, 6–8 and 9–11 correspond to 2D pillars, fibers and sinusoid topographies, respectively (see table 1). Reproduced from [67]. © IOP Publishing Ltd. All rights reserved).

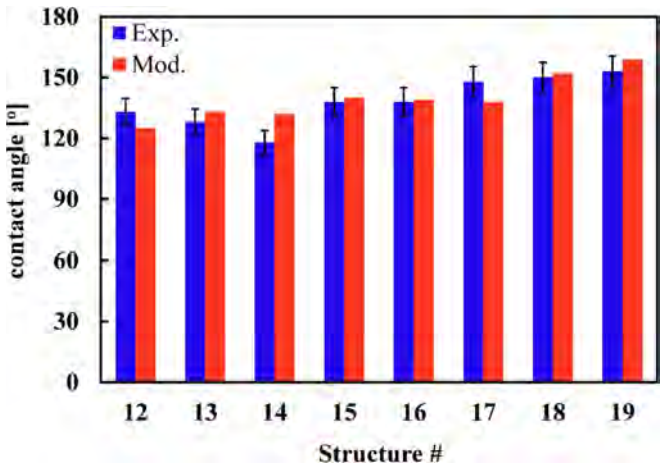

Figure 4. Contact angle comparison between model results (red) and experimental data (blue) for eight single-level topographies with 3D-pillars texture (see table 1 and figure 1).

tested structures displaying this topography within the uncertainties of the experimental data. The model results for the fiber topography, shown in figure 3, were substantially closer to their experimental counterparts giving rise to an average error below 3%. Clearly, figure 3 shows that the attained contact angles for the fiber topography were larger than the ones for 2D pillars, thereby corroborating previous modeling observations and associated trends [67] relating this behavior with the re-entrant geometry of the fiber topography.

The calculated contact angles for the sinusoidal topography were substantially smaller than the previous two single-level topographies, namely 2D pillars and fibers. This observation becomes apparent by juxtaposing the three topographies shown in figure 3 and is in excellent agreement with recent theoretical predictions identifying fibers as the most efficacious amongst the three single-level topographies for achieving high contact angles, followed, in order of efficiency, by 2D pillars and finally sinusoidal surfaces [67]. Figure 3 shows that the agreement between experimental measurements and model predictions for sinusoidal topographies was remarkably good exhibiting an average error of only 4.6%.

Next, consideration of actual 3D surface topographies, instead of simplified semi-infinite 2D structures, resulted in increased water contact angles and thus enhanced water repellency. This behavior is illustrated in figure 4 for the 3D-pillars case and was attributed to an augmented surface-to-volume ratio, generally more pronounced in 3D structures than in commensurate 2D topographies, inducing thereby increased surface roughness and thus enhanced liquid-repellency. The predicted contact angles were, once again, in reasonable accord with experimental observations displaying average deviations of not more than 4.5%. Taken all together, predicted contact

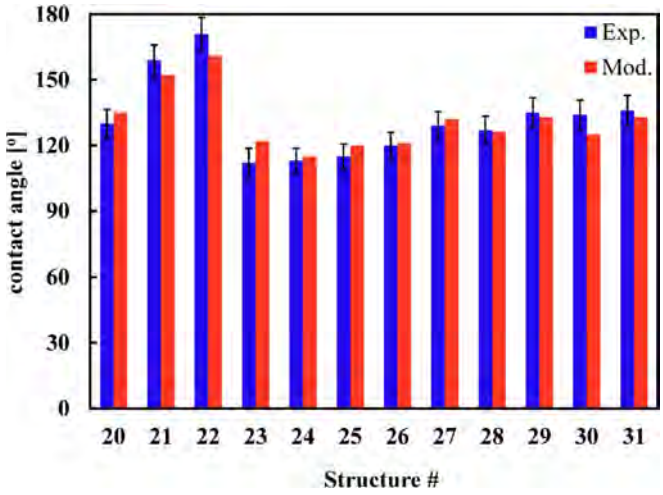

Figure 5. Contact angle comparison between model results (red) and experimental data (blue) for twelve two-level surface topographies: Structures 20–22 describe 'pillars on sinusoids', whereas structures 23–31 correspond to 'sinusoids on sinusoids' topographies. (see table 2).

angles for the four types of single-level topographies considered here (see table 1) deviated, on average, from experimental measurements by less than 5%. This discrepancy was, for most surface topographies examined here, within the statistical uncertainties of experimental data.

3.2. Multilevel topographies

It is well established in the literature that multilevel hierarchical surface topographies induced enhanced liquid repellency. Figure 5 validates this consensus by illustrating calculated and experimentally measured contact angles for two types of two-level topography. For most structures in figure 5, contact angles lay in the vicinity of 140°, with two surfaces exhibiting superhydrophobic behavior ($\theta > 150°$). Structures 20–22 in figure 5 correspond to two-level topographies featuring pillars (fine level) on top of sinusoids (coarse level), wherein the two levels differed in size by at least one order of magnitude (see table 2). This observation validates previous theoretical findings arguing that a size difference of at least one order of magnitude between the superimposed surface patterns was required for achieving superhydrophobicity [67]. Notwithstanding the significance and influence of multilevel hierarchical structures on liquid repellency, the construction of such surfaces poses substantial technological challenges. This is due to the intrinsic technological difficulties associated with manufacturing of surface details on the submicron or even nanoscale.

Structures 23–31 in figure 5 correspond to 'sinusoids on sinusoids' two-level topographies giving rise to contact angles consistently smaller than the ones for 'pillars on sinusoids' surfaces. Given that the surface material was in both cases the same (PDMS), the coarse level was of the same type (sinusoids) and, more or less, on the same order of magnitude (table 2), we discerned that the behavior of two-level topographies was greatly influenced by the upper (finer) level. According to the single-level results reported in section 3.1, 2D-pillar surfaces exhibited, in general, larger contact angles than sinusoidal topographies. The behavior shown in figure 5 is, therefore, consistent with this observation. For both types of two-level topography considered here, the calculated contact angles were in notable accord with their experimental counterparts. The average deviation for the 'pillars on sinusoids' and 'sinusoids on sinusoids' topographies amounted to 4.7% and 3.2%, respectively, resulting in an average deviation of 4% for the two-level topographies.

Finally, figure 6 shows the comparison between the predicted and the experimental contact angle for a three-level topography with three levels of sinusoid, each having dimensions that differed by one order of magnitude from the next one (table 2). Superhydrophobicity was observed here as well, further validating the general belief that multilevel topographies enable increased liquid-repellency. Indeed, this becomes clear by comparing the contact angles for sinusoidal single-, two- and three-level topographies shown in figure 3 (structures 9–11), 4 (structures 23–31) and 5, respectively. The addition of a second level of sinusoidal patterns almost doubled the observed contact angle, while incorporation of a third sinusoidal level brought about an additional 12.5% contact angle increase. Again, our model predicted for this three-level surface topography a contact angle that deviated only by 3.1% from the experimentally measured value, well within the statistical uncertainty of the experimental measurement. Taken all together, figures 5, 6 and the discussion therein confirmed the ability of our model to predict very accurately the wetting behavior of surfaces exhibiting multilevel hierarchical topographies.

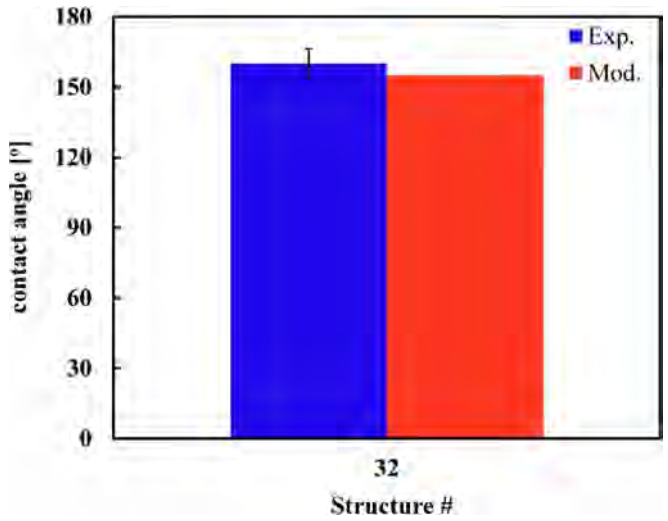

Figure 6. Contact angle comparison between model results (red) and experimental data (blue) for a three-level surface topography corresponding to three levels of sinusoids placed on top of each other (see table 2).

4. Conclusions

The objective of this work is twofold; on one side, we report the extension of the formalism of our recently published wetting model [67] to account for 3D pillar topographies, while, on the other hand, we provide compelling evidence on the validation of our model in capturing accurately the wetting behavior across various topography types, surface materials and hierarchy levels. Realistic engineered surfaces featuring single-, two- and three-level surface topographies, found either in the literature or fabricated and analyzed in the context of this work, were utilized for validation purposes. One-to-one comparison between modeling results and experimental data validated our original theoretical hypothesis that, in general, multilevel hierarchical topographies enable enhanced liquid-repellency, constituting thereby a valuable tool for achieving superhydrophobicity.

Of the four single-level surface topographies considered here, the 3D pillars exhibited the highest contact angles, in some cases exceeding 150°, owed to increased surface-to-volume ratio compared to the commensurate semi-infinite 2D textures. Subsequently, the fiber topography, presenting re-entrant geometry, yielded the largest contact angles among the single level 2D topographies, followed by the 2D pillars and sinusoidal topographies. Increased water repellency was, in general, observed for two-level hierarchical surfaces, while three-level sinusoidal hierarchical surfaces yielded contact angles as high as 165°. For the three-level sinusoidal topography, addition of a second level of sinusoidal patterns almost doubled the observed contact angle, while incorporation of a third sinusoidal level brought about an additional 12.5% contact angle increase. In all cases of multilevel topographies considered here, the different superposing levels had length scales differing in size from one another by at least one order of magnitude.

Our model predictions were for all single-level topographies considered here in gratifying agreement with experimental contact angle measurements resulting to an average error of 4.6%, well within the experimental statistical uncertainty. Analogous comparisons for two- and three-level topographies resulted in average deviations of about 3.5%. Taken all together, our refined wetting model captured remarkably well and within experimental inaccuracies the wetting behavior of water on various materials exhibiting single- and multilevel hierarchical roughness. Modelling wettability accurately across different wetting liquids, surface materials and topographies sets the foundations of a generic surface design methodology enabling tailored wetting properties for numerous technological applications relevant to packaging, circular economy of materials, waste reduction, recycling, as well as conservation of energy and natural resources.

Acknowledgments

NL and RK gratefully acknowledge the University of Applied Sciences Western Switzerland (HES-SO), the College of Engineering and Architecture Fribourg (HEIA-FR) and the MARKETPLACE (Materials Modelling Marketplace for Increased Industrial Innovation) project funded by the Horizon 2020 EU program under the NMBP-25-2017 call, with Grant agreement number 760173 (https:/the-marketplace-project.eu/) for financial support. PMK gratefully acknowledges the Swiss Nanoscience Institute (SNI) for funding of the projects PATCELL and REPALL with grant numbers 09.10 and 10.07, respectively, under the framework of the Nanoargovia program. RDA acknowledges funding from the BIOSMART project

belonging to the Bio Based Industries Joint Undertaking under the European Union's Horizon 2020 - Research and Innovation Framework Program with Grant agreement number 745762. Computational time and resources for this work were granted by the Department of Computer Science and Communication Systems at HEIA-FR.

Data availability statement

The data that support the findings of this study are available upon reasonable request from the authors.

ORCID iDs

Nikolaos Lempesis https://orcid.org/0000-0002-4104-9666
Ruth Díez-Ahedo https://orcid.org/0000-0002-8033-0792
Per Magnus Kristiansen https://orcid.org/0000-0001-7714-0966

References

[1] Adhikari B, Howes T, Bhandari B R and Truong V 2001 Stickiness in foods: a review of mechanisms and test methods *Int. J. Food Prop.* **4** 1–33
[2] Harte B R, Gray J I and Miltz J 1987 *Food Product-Package Compatibility* (Michigan State University: East Lansing: CRC Press)
[3] Michalski M C, Desobry S and Hardy J 1997 Food materials adhesion: a review *Crit. Rev. Food Sci. Nutr.* **37** 591–619
[4] Criado M, Suárez B and Ferreirós C 1994 The importance of bacterial adhesion in the dairy industry *Food Technology* **48** 123–6
[5] Nosonovsky M and Bhushan B 2008 Roughness-induced superhydrophobicity: a way to design non-adhesive surfaces *J. Phys. Condens. Matter* **20** 225009
[6] Höcker H 2002 Plasma treatment of textile fibers *Pure Appl. Chem.* **74** 423–7
[7] Zimmermann J, Reifler F A, Fortunato G, Gerhardt L-C and Seeger S 2008 A simple, one-step approach to durable and robust superhydrophobic textiles *Adv. Funct. Mater.* **18** 3662–9
[8] Shabanian S, Khatir B, Nisar A and Golovin K 2020 Rational design of perfluorocarbon-free oleophobic textiles *Nature Sustainability* **3** 1059–66
[9] Gao X, Yan X, Yao X, Xu L, Zhang K, Zhang J, Yang B and Jiang L 2007 The dry-style antifogging properties of mosquito compound eyes and artificial analogues prepared by soft lithography *Adv. Mater.* **19** 2213–7
[10] Cao L, Jones A K, Sikka V K, Wu J and Gao D 2009 Anti-icing superhydrophobic coatings *Langmuir* **25** 12444–8
[11] Pan Q and Wang M 2009 Miniature boats with striking loading capacity fabricated from superhydrophobic copper meshes *ACS Appl. Mater. Interfaces* **1** 420–3
[12] Ou J, Perot B and Rothstein J P 2004 Laminar drag reduction in microchannels using ultrahydrophobic surfaces *Phys. Fluids* **16** 4635–43
[13] Marmur A 2006 Underwater Superhydrophobicity: theoretical feasibility *Langmuir* **22** 1400–2
[14] Gurera D and Bhushan B 2019 Optimization of bioinspired conical surfaces for water collection from fog *J. Colloid Interface Sci.* **551** 26–38
[15] Wilson S J and Hutley M C 1982 The optical properties of'moth eye'antireflection surfaces *Optica Acta: International Journal of Optics* **29** 993–1009
[16] Carlo M and Metin S 2006 A biomimetic climbing robot based on the gecko *J. Bionic Eng.* **3** 115–25
[17] Arzt E, Gorb S and Spolenak R 2003 From micro to nano contacts in biological attachment devices *Proc. Natl Acad. Sci.* **100** 10603
[18] Solga A, Cerman Z, Striffler B F, Spaeth M and Barthlott W 2007 The dream of staying clean: Lotus and biomimetic surfaces *Bioinsp. Biomim.* **2** S126
[19] Dean B and Bhushan B 2010 Shark-skin surfaces for fluid-drag reduction in turbulent flow: a review *Philosophical Transactions of the Royal Society A: Mathematical, Physical and Engineering Sciences* **368** 4775–806
[20] Bushnell D M and Moore K J 1991 Drag reduction in nature *Annual Review of Fluid Mechanics* **23** 65–79
[21] Nosonovsky M and Bhushan B 2009 Superhydrophobic surfaces and emerging applications: non-adhesion, energy, green engineering *Current Opinion in Colloid & Interface Science* **14** 270–80
[22] Nakajima A, Fujishima A, Hashimoto K and Watanabe T 1999 Preparation of transparent superhydrophobic boehmite and silica films by sublimation of aluminum acetylacetonate *Adv. Mater.* **11** 1365–8
[23] Chen W, Fadeev A Y, Hsieh M C, Öner D, Youngblood J and McCarthy T J 1999 Ultrahydrophobic and ultralyophobic surfaces: some comments and examples *Langmuir* **15** 3395–9
[24] Kijlstra J, Reihs K and Klamt A 2002 Roughness and topology of ultra-hydrophobic surfaces *Colloids Surf.*, A **206** 521–9
[25] Herminghaus S 2000 Roughness-induced non-wetting *EPL (Europhysics Letters)* **52** 165
[26] Sun T, Wang G, Feng L, Liu B, Ma Y, Jiang L and Zhu D 2004 Reversible switching between superhydrophilicity and superhydrophobicity *Angew. Chem. Int. Ed.* **43** 357–60
[27] Zhang J, Lu X, Huang W and Han Y 2005 Reversible superhydrophobicity to superhydrophilicity transition by extending and unloading an elastic polyamide film *Macromol. Rapid Commun.* **26** 477–80
[28] Lu X, Zhang C and Han Y 2004 Low-density polyethylene superhydrophobic surface by control of its crystallization behavior *Macromol. Rapid Commun.* **25** 1606–10
[29] Seemann R, Brinkmann M, Herminghaus S, Khare K, Law B M, McBride S, Kostourou K, Gurevich E, Bommer S and Herrmann C 2011 Wetting morphologies and their transitions in grooved substrates *J. Phys. Condens. Matter* **23** 184108
[30] Khare K, Brinkmann M, Law B M, Herminghaus S and Seemann R 2009 Switching wetting morphologies in triangular grooves *Eur. Phys. J. Spec. Top.* **166** 151–4
[31] Nishino T, Meguro M, Nakamae K, Matsushita M and Ueda Y 1999 The lowest surface free energy based on −CF3 alignment *Langmuir* **15** 4321–3
[32] Tuteja A, Choi W, Ma M, Mabry J M, Mazzella S A, Rutledge G C, McKinley G H and Cohen R E 2007 Designing superoleophobic surfaces *Science* **318** 1618–22
[33] Chauhan P, Kumar A and Bhushan B 2019 Self-cleaning, stain-resistant and anti-bacterial superhydrophobic cotton fabric prepared by simple immersion technique *J. Colloid Interface Sci.* **535** 66–74
[34] Li F, Bhushan B, Pan Y and Zhao X 2019 Bioinspired superoleophobic/superhydrophilic functionalized cotton for efficient separation of immiscible oil-water mixtures and oil-water emulsions *J. Colloid Interface Sci.* **548** 123–30
[35] Nanda D, Sahoo A, Kumar A and Bhushan B 2019 Facile approach to develop durable and reusable superhydrophobic/superoleophilic coatings for steel mesh surfaces *J. Colloid Interface Sci.* **535** 50–7
[36] Gurera D and Bhushan B 2018 Fabrication of bioinspired superliquiphobic synthetic leather with self-cleaning and low adhesion *Colloids Surf.* A **545** 130–7
[37] Alinezhadfar M, Nasiri Khalil Abad S and Mozammel M 2020 Multifunctional cobalt coating with exceptional amphiphobic

properties: self-cleaning and corrosion inhibition *Surfaces and Interfaces* **21** 100744
[38] Nasiri Khalil Abad S, Najibi Ilkhechi N, Adel M and Mozammel M 2020 Hierarchical architecture of a superhydrophobic Cd-Si co-doped TiO_2 thin film *Appl. Surf. Sci.* **533** 147495
[39] Nasiri Khalil Abad S, Mozammel M, Moghaddam J, Mostafaei A and Chmielus M 2020 Highly porous, flexible and robust cellulose acetate/Au/ZnO as a hybrid photocatalyst *Appl. Surf. Sci.* **526** 146237
[40] Bhushan B and Martin S 2018 Substrate-independent superliquiphobic coatings for water, oil, and surfactant repellency: an overview *J. Colloid Interface Sci.* **526** 90–105
[41] Tuteja A, Choi W, Mabry J M, McKinley G H and Cohen R E 2008 Robust omniphobic surfaces *Proc. Natl Acad. Sci.* **105** 18200
[42] Cheng Y-T and Rodak D E 2005 Is the lotus leaf superhydrophobic? *Appl. Phys. Lett.* **86** 144101
[43] Marmur A 2003 Wetting on hydrophobic rough surfaces: to be heterogeneous or Not To Be? *Langmuir* **19** 8343–8
[44] Nosonovsky M 2007 Multiscale roughness and stability of superhydrophobic biomimetic interfaces *Langmuir* **23** 3157–61
[45] Bittoun E and Marmur A 2012 The role of multiscale roughness in the lotus effect: is it essential for super-hydrophobicity? *Langmuir* **28** 13933–42
[46] Nosonovsky M and Bhushan B 2008 Biologically inspired surfaces: broadening the scope of roughness *Adv. Funct. Mater.* **18** 843–55
[47] Zhai L, Cebeci F C, Cohen R E and Rubner M F 2004 Stable superhydrophobic coatings from polyelectrolyte multilayers *Nano Lett.* **4** 1349–53
[48] Chhatre S S, Choi W and Tuteja A 2010 Scale dependence of omniphobic mesh surfaces *Langmuir* **26** 4027–35
[49] Ma M and Hill R M 2006 Superhydrophobic surfaces *Current opinion in colloid & interface science* **11** 193–202
[50] Barbieri L, Wagner E and Hoffmann P 2007 Water wetting transition parameters of perfluorinated substrates with periodically distributed flat-top microscale obstacles *Langmuir* **23** 1723–34
[51] Kang S M, You I, Cho W K, Shon H K, Lee T G, Choi I S, Karp J M and Lee H 2010 One-step modification of superhydrophobic surfaces by a mussel-inspired polymer coating *Angew. Chem. Int. Ed.* **49** 9401–4
[52] Young T 1805 III An essay on the cohesion of fluids *Philosophical Transactions of the Royal Society of London* **95** 65–87
[53] Wenzel R N 1936 Resistance of solid surfaces to wetting by water *Industrial & Engineering Chemistry* **28** 988–94
[54] Cassie A B D and Baxter S 1944 Wettability of porous surfaces *Trans. Faraday Soc.* **40** 546–51
[55] Afferrante L and Carbone G 2010 Microstructured superhydrorepellent surfaces: effect of drop pressure on fakir-state stability and apparent contact angles *J. Phys. Condens. Matter* **22** 325107
[56] Afferrante L and Carbone G 2014 The effect of drop volume and micropillar shape on the apparent contact angle of ordered microstructured surfaces *Soft Matter* **10** 3906–14
[57] Afferrante L and Carbone G 2015 Statistical theory of wetting of liquid drops on superhydrophobic randomly rough surfaces *Phys. Rev.* E **92** 042407
[58] Ciavarella M and Afferrante L 2016 Adhesion of rigid rough contacts with bounded distribution of heights *Tribol. Int.* **100** 18–23
[59] Jung M, Brinkmann M, Seemann R, Hiller T, Sanchez de La Lama M and Herminghaus S 2016 Wettability controls slow immiscible displacement through local interfacial instabilities *Phys. Rev. Fluids* **1** 074202
[60] Violano G and Afferrante L 2019 Contact of rough surfaces: modeling adhesion in advanced multiasperity models *Proc. Inst. Mech. Eng. Part J J. Eng. Tribol.* **233** 1585–93
[61] Marmur A and Bittoun E 2009 When wenzel and cassie are right: reconciling local and global considerations *Langmuir* **25** 1277–81
[62] Bittoun E and Marmur A 2010 Chemical nano-heterogeneities detection by contact angle hysteresis: theoretical feasibility *Langmuir* **26** 15933–7
[63] Carbone G and Mangialardi L 2005 Hydrophobic properties of a wavy rough substrate *The European Physical Journal* E **16** 67–76
[64] Bottiglione F and Carbone G 2013 Role of statistical properties of randomly rough surfaces in controlling superhydrophobicity *Langmuir* **29** 599–609
[65] Brown P S and Bhushan B 2016 Designing bioinspired superoleophobic surfaces *APL Mater.* **4** 015703
[66] Brown P S and Bhushan B 2016 Durable, superoleophobic polymer–nanoparticle composite surfaces with re-entrant geometry via solvent-induced phase transformation *Sci. Rep.* **6** 21048
[67] Lempesis N, Janka A, Gnatiuk O, van Eijndhoven S J L and Koopmans R J 2020 Predicting bio-inspired candidate surfaces with superomniphobic characteristics *Surf. Topogr.: Metrol. Prop.* **8** 025021
[68] Vázquez U O M, Shinoda W, Moore P B, Chiu C-C and Nielsen S O 2009 Calculating the surface tension between a flat solid and a liquid: a theoretical and computer simulation study of three topologically different methods *J. Math. Chem.* **45** 161–74
[69] Zisman W A 1964 *Contact Angle, Wettability, and Adhesion* (Washington, DC: American Chemical Society) pp 1–51
[70] Owens D K and Wendt R C 1969 Estimation of the surface free energy of polymers *J. Appl. Polym. Sci.* **13** 1741–7
[71] Ayyoob M and Kim Y J 2018 Effect of chemical composition variant and oxygen plasma treatments on the wettability of PLGA thin films, synthesized by direct copolycondensation *Polymers (Basel)* **10** 1132
[72] Cheng C T, Zhang G and To S 2016 Wetting characteristics of bare micro-patterned cyclic olefin copolymer surfaces fabricated by ultra-precision raster milling *RSC Adv.* **6** 1562–70
[73] Lv T, Cheng Z, Zhang D, Zhang E, Zhao Q, Liu Y and Jiang L 2016 Superhydrophobic surface with shape memory Micro/Nanostructure and its application in rewritable chip for droplet storage *ACS Nano* **10** 9379–86
[74] Lee S G, Lee D Y, Lim H S, Lee D H, Lee S and Cho K 2010 Switchable transparency and wetting of elastomeric smart windows *Adv. Mater.* **22** 5013–7
[75] Lin G, Zhang Q, Lv C, Tang Y and Yin J 2018 Small degree of anisotropic wetting on self-similar hierarchical wrinkled surfaces *Soft Matter* **14** 1517–29
[76] Lee W-K, Jung W-B, Nagel S R and Odom T W 2016 Stretchable superhydrophobicity from monolithic, three-dimensional hierarchical wrinkles *Nano Lett.* **16** 3774–9